An Improved Iterative Neural Network for High-Quality Image-Domain Material Decomposition in Dual-Energy CT – Supplementary Material

This supplement provides details for optimizing the training loss function in (P1), relation between convolution-perspective and patch-based trainings for distinct cross-material CNN refiner in (1), and additional experimental results to accompany our main manuscript[1]. We use the prefix "S" for the numbers in section, proposition, equation, and figure in the supplementary material.

S.I Optimizing (P1) with a Mini-Batch Stochastic Gradient Method

The training loss at each mini-batch is

$$\begin{aligned}\mathcal{L} =& \frac{1}{B}\sum_{r=1}^{2R}\sum_{b=1}^{B}\left(X_{rb} - \mathbf{D}_r \mathcal{T}_{\exp(\boldsymbol{\alpha})}\left(\mathbf{E}\mathbf{X}_b^{(i-1)}\right)\right)^2 \\ =& \sum_{r=1}^{2R}\sum_{b=1}^{B}\frac{1}{B}\left[X_{rb} - \mathbf{D}_r\left(\sum_{r=1}^{2R}\mathbf{E}_r X_{rb}^{(i-1)} - \exp(\boldsymbol{\alpha})\odot \ \mathrm{sign}\left(\sum_{r=1}^{2R}\mathbf{E}_r X_{rb}^{(i-1)}\right)\right)\odot \mathbb{1}_{|\mathbf{E}\mathbf{X}_b^{(i-1)}|>\exp(\boldsymbol{\alpha})}\right]^2,\end{aligned}$$

where $\mathbf{D}_r$ is the rth row of $\mathbf{D}$, $\mathbf{E}_r$ is the rth column of $\mathbf{E}$, $(\cdot)_{rb}$ denotes the element at rth row and bth column of the matrix. Therefore, subgradient of (P1) with respect to $\boldsymbol{\alpha}$ at each mini-batch is

$$\begin{aligned}&\frac{\partial \mathcal{L}(\mathbf{D},\,\mathbf{E},\,\boldsymbol{\alpha})}{\partial \boldsymbol{\alpha}} = \frac{2}{B}\sum_{r=1}^{2R}\sum_{b=1}^{B}\left[X_{rb} - \mathbf{D}_r\mathcal{T}_{\exp(\boldsymbol{\alpha})}\left(\mathbf{E}\mathbf{X}_b^{(i-1)}\right)\right]\cdot \\ &\frac{\partial \mathbf{D}_r\left[\exp(\boldsymbol{\alpha})\odot \mathrm{sign}\left(\sum_{r=1}^{2R}\mathbf{E}_r X_{rb}^{(i-1)}\right)\right]\odot \mathbb{1}_{|\mathbf{E}\mathbf{X}_b^{(i-1)}|>\exp(\boldsymbol{\alpha})}}{\partial \boldsymbol{\alpha}} \\ =&\frac{2}{B}\sum_{r=1}^{2R}\sum_{b=1}^{B}\left[X_{rb} - \mathbf{D}_r\mathcal{T}_{\exp(\boldsymbol{\alpha})}\left(\mathbf{E}\mathbf{X}_b^{(i-1)}\right)\right]\cdot \mathbf{D}_r^\top \odot \exp(\boldsymbol{\alpha})\odot \mathrm{sign}\left(\mathbf{E}\mathbf{X}_b^{(i-1)}\right)\odot \mathbb{1}_{|\mathbf{E}\mathbf{X}_b^{(i-1)}|>\exp(\boldsymbol{\alpha})} \\ =&\frac{2}{B}\left\{\mathbf{D}^\top\left(\mathbf{X}-\mathbf{D}\mathbf{Z}^{(i-1)}\right)\odot \exp(\boldsymbol{\alpha}\mathbf{1}')\odot \mathrm{sign}\left(\mathbf{E}\mathbf{X}^{(i-1)}\right)\odot\ \mathbb{1}_{|\mathbf{E}\mathbf{X}^{(i-1)}|>\exp(\boldsymbol{\alpha}\mathbf{1}')}\right\}\mathbf{1} \\ =&\frac{2}{B}\left\{\mathbf{D}^\top\left(\mathbf{X}-\mathbf{D}\mathbf{Z}^{(i-1)}\right)\odot \exp(\boldsymbol{\alpha}\mathbf{1}')\odot \mathrm{sign}\left(\mathbf{Z}^{(i-1)}\right)\right\}\mathbf{1}.\end{aligned}$$

We can easily obtain subgradient of $\mathcal{L}$ with respect to $\mathbf{D}$ at each mini-batch as

$$\frac{\partial \mathcal{L}}{\partial \mathbf{D}} = -\frac{2}{B}\left(\mathbf{X} - \mathbf{D}\mathbf{Z}^{(i-1)}\right) \cdot \mathbf{Z}^{(i-1)^\top}.$$

At each mini-batch, the subgradient of $\mathcal{L}$ with respect to r_1th column of $\mathbf{E}$ is as follows:

$$\frac{\partial \mathcal{L}(\mathbf{D}, \mathbf{E}, \boldsymbol{\alpha})}{\partial \mathbf{E}_{r_1}} = -\frac{2}{B}\sum_{r=1}^{2R}\sum_{b=1}^{B}\left(X_{rb} - \mathbf{D}_r \mathcal{T}_{\exp(\boldsymbol{\alpha})}\left(\mathbf{E}\mathbf{X}_b^{(i-1)}\right)\right) \cdot \quad \mathbf{D}_r^\top \odot \mathbb{1}_{|\mathbf{E}\mathbf{X}_b^{(i-1)}|>\exp(\boldsymbol{\alpha})} \cdot X_{r_1 b}^{(i-1)}$$
$$= -\frac{2}{B}\sum_{b=1}^{B}\mathbf{D}^\top\left(\mathbf{X}_b - \mathbf{D}\mathcal{T}_{\exp(\boldsymbol{\alpha})}\left(\mathbf{E}\mathbf{X}_b^{(i-1)}\right)\}\right) \odot \mathbb{1}_{|\mathbf{E}\mathbf{X}_b^{(i-1)}|>\exp(\boldsymbol{\alpha})} \cdot X_{r_1 b}^{(i-1)}$$
$$= -\frac{2}{B}\mathbf{D}^\top\left(\mathbf{X} - \mathbf{D}\mathbf{Z}^{(i-1)}\right) \odot \mathbb{1}_{|\mathbf{E}\mathbf{X}^{(i-1)}|>\exp(\boldsymbol{\alpha}\mathbf{1}')} \cdot \mathbf{X}_{r_1}^{(i-1)^\top}.$$

Thus, the subgradient of $\mathcal{L}$ with respect to $\mathbf{E}$ for each mini-batch selection is

$$\frac{\partial \mathcal{L}(\mathbf{D}, \mathbf{E}, \boldsymbol{\alpha})}{\partial \mathbf{E}} = -\frac{2}{B}\mathbf{D}^\top\left(\mathbf{X} - \mathbf{D}\mathcal{T}_{\exp(\boldsymbol{\alpha}\mathbf{1}')}\left(\mathbf{E}\mathbf{X}^{(i-1)}\right)\right) \odot \mathbb{1}_{|\mathbf{E}\mathbf{X}^{(i-1)}|>\exp(\boldsymbol{\alpha}\mathbf{1}')} \cdot \mathbf{X}^{(i-1)^\top}$$

S.II Relation between convolution-perspective and patch-based trainings of the proposed BCD-Net-sCNN-hc

Proposition S.1 *The proposed CNN refiner in (1) can be rewritten with patch-based perspective as follows (we omit the iteration superscript indices (i) for simplicity):*

$$\begin{bmatrix} \sum_{k=1}^{K}\sum_{n=1}^{2}\mathbf{d}_{1,n,k} * \mathcal{T}_{\exp(\alpha_{n,k})}\left(\sum_{m=1}^{2}\mathbf{e}_{n,m,k} * \mathbf{x}_m\right) \\ \sum_{k=1}^{K}\sum_{n=1}^{2}\mathbf{d}_{2,n,k} * \mathcal{T}_{\exp(\alpha_{n,k})}\left(\sum_{m=1}^{2}\mathbf{e}_{n,m,k} * \mathbf{x}_m\right) \end{bmatrix} = \frac{1}{R}\sum_{j=1}^{N}\bar{\mathbf{P}}_j^\top \mathbf{D}\mathcal{T}_{\exp(\boldsymbol{\alpha})}(\mathbf{E}\bar{\mathbf{P}}_j\mathbf{x}), \quad \text{(S.1)}$$

where $\mathbf{x} = [\mathbf{x}_1^\top, \mathbf{x}_2^\top]^\top$. See other related notations in (1) and (5).

Proof. First, we have the following reformulation[2]:

$$\begin{bmatrix} \mathbf{e}_{n,m,1} * \mathbf{u} \\ \vdots \\ \mathbf{e}_{n,m,K} * \mathbf{u} \end{bmatrix} = \mathbf{P}\begin{bmatrix} \mathbf{E}_{n,m}\mathbf{P}_1 \\ \vdots \\ \mathbf{E}_{n,m}\mathbf{P}_N \end{bmatrix}\mathbf{u} := \widetilde{\mathbf{E}}_{n,m}\mathbf{u},$$

where $\mathbf{P} \in \mathbb{R}^{KN \times KN}$ is a permutation matrix. Considering that

$$\sum_{k=1}^{K} \bar{\mathbf{e}}_{n,m,k} * (\mathbf{e}_{n,m,k} * \mathbf{u}) = \frac{1}{R} \widetilde{\mathbf{E}}_{n,m}^{H} \widetilde{\mathbf{E}}_{n,m} \mathbf{u},$$

we have

$$\sum_{k=1}^{K} \mathbf{d}_{1,1,k} * (\mathbf{e}_{1,1,k} * \mathbf{x}_1) = \frac{1}{R} \widetilde{\mathbf{D}}_{1,1} \widetilde{\mathbf{E}}_{1,1} \mathbf{x}_1 \quad \text{and} \quad \sum_{k=1}^{K} \mathbf{d}_{1,1,k} * (\mathbf{e}_{1,2,k} * \mathbf{x}_2) = \frac{1}{R} \widetilde{\mathbf{D}}_{1,1} \widetilde{\mathbf{E}}_{1,2} \mathbf{x}_2.$$

Then we obtain the following reformulation result for term $\sum_{k=1}^{K} \mathbf{d}_{1,1,k} * \mathcal{T}_{\exp(\alpha_{1,k})}(\mathbf{e}_{1,1,k} * \mathbf{x}_1 + \mathbf{e}_{1,2,k} * \mathbf{x}_2)$:

$$\sum_{k=1}^{K} \mathbf{d}_{1,1,k} * \mathcal{T}_{\exp(\alpha_{1,k})} \left(\mathbf{e}_{1,1,k} * \mathbf{x}_1 + \mathbf{e}_{1,2,k} * \mathbf{x}_2 \right) = \frac{1}{R} \sum_{j=1}^{N} \mathbf{P}_j^{\top} \mathbf{D}_{1,1} \mathcal{T}_{\exp(\boldsymbol{\alpha}_1)} \left(\mathbf{E}_{1,1} \mathbf{P}_j \mathbf{x}_1 + \mathbf{E}_{1,2} \mathbf{P}_j \mathbf{x}_2 \right), \tag{S.2}$$

where we use the permutation invariance of thresholding operator[3] and $\mathbf{P}^{\top}\mathbf{P} = \mathbf{I}$. Similarly, for term $\sum_{k=1}^{K} \mathbf{d}_{1,2,k} * \mathcal{T}_{\exp(\alpha_{2,k})}(\mathbf{e}_{2,1,k} * \mathbf{x}_1 + \mathbf{e}_{2,2,k} * \mathbf{x}_2)$, we have

$$\sum_{k=1}^{K} \mathbf{d}_{1,2,k} * \mathcal{T}_{\exp(\alpha_{2,k})} \left(\mathbf{e}_{2,1,k} * \mathbf{x}_1 + \mathbf{e}_{2,2,k} * \mathbf{x}_2 \right) = \frac{1}{R} \sum_{j=1}^{N} \mathbf{P}_j^{\top} \mathbf{D}_{1,2} \mathcal{T}_{\exp(\boldsymbol{\alpha}_2)} \left(\mathbf{E}_{2,1} \mathbf{P}_j \mathbf{x}_1 + \mathbf{E}_{2,2} \mathbf{P}_j \mathbf{x}_2 \right). \tag{S.3}$$

Combining (S.2) and (S.3) gives the following result:

$$\begin{aligned} \sum_{k=1}^{K} \sum_{n=1}^{2} \mathbf{d}_{1,n,k} * \mathcal{T}_{\exp(\alpha_{n,k})} \left(\sum_{m=1}^{2} \mathbf{e}_{n,m,k} * \mathbf{x}_m \right) = \frac{1}{R} \sum_{j=1}^{N} \mathbf{P}_j^{\top} \mathbf{D}_{1,1} \mathcal{T}_{\exp(\boldsymbol{\alpha}_1)} \left(\mathbf{E}_{1,1} \mathbf{P}_j \mathbf{x}_1 + \mathbf{E}_{1,2} \mathbf{P}_j \mathbf{x}_2 \right) + \\ \frac{1}{R} \sum_{j=1}^{N} \mathbf{P}_j^{\top} \mathbf{D}_{1,2} \mathcal{T}_{\exp(\boldsymbol{\alpha}_2)} \left(\mathbf{E}_{2,1} \mathbf{P}_j \mathbf{x}_1 + \mathbf{E}_{2,2} \mathbf{P}_j \mathbf{x}_2 \right). \end{aligned} \tag{S.4}$$

Similar to (S.4), we have

$$\begin{aligned} \sum_{k=1}^{K} \sum_{n=1}^{2} \mathbf{d}_{2,n,k} * \mathcal{T}_{\exp(\alpha_{n,k})} \left(\sum_{m=1}^{2} \mathbf{e}_{n,m,k} * \mathbf{x}_m \right) = \frac{1}{R} \sum_{j=1}^{N} \mathbf{P}_j^{\top} \mathbf{D}_{2,1} \mathcal{T}_{\exp(\boldsymbol{\alpha}_1)} \left(\mathbf{E}_{1,1} \mathbf{P}_j \mathbf{x}_1 + \mathbf{E}_{1,2} \mathbf{P}_j \mathbf{x}_2 \right) + \\ \frac{1}{R} \sum_{j=1}^{N} \mathbf{P}_j^{\top} \mathbf{D}_{2,2} \mathcal{T}_{\exp(\boldsymbol{\alpha}_2)} \left(\mathbf{E}_{2,1} \mathbf{P}_j \mathbf{x}_1 + \mathbf{E}_{2,2} \mathbf{P}_j \mathbf{x}_2 \right). \end{aligned} \tag{S.5}$$

Combining the results in (S.4) and (S.5) completes the proof.

Proposition S.2 *The loss function for training the proposed CNN refiner in (1) is bounded by its patch-based training loss function:*

$$\begin{aligned}\frac{1}{2L}\sum_{l=1}^{L}\left\|\begin{bmatrix}\mathbf{x}_{l,1}\\ \mathbf{x}_{l,2}\end{bmatrix}-\begin{bmatrix}\sum_{k=1}^{K}\sum_{n=1}^{2}\mathbf{d}_{1,n,k}*\mathcal{T}_{\exp(\alpha_{n,k})}\left(\sum_{m=1}^{2}\mathbf{e}_{n,m,k}*\mathbf{x}_{l,m}^{(i-1)}\right)\\ \sum_{k=1}^{K}\sum_{n=1}^{2}\mathbf{d}_{2,n,k}*\mathcal{T}_{\exp(\alpha_{n,k})}\left(\sum_{m=1}^{2}\mathbf{e}_{n,m,k}*\mathbf{x}_{l,m}^{(i-1)}\right)\end{bmatrix}\right\|_2^2 \leq \\ \frac{1}{2LR}\sum_{l=1}^{L}\left\|\begin{bmatrix}\widetilde{\mathbf{X}}_{l,1}\\ \widetilde{\mathbf{X}}_{l,2}\end{bmatrix}-\mathbf{D}\mathcal{T}_{\exp(\boldsymbol{\alpha})}\left(\mathbf{E}\begin{bmatrix}\widetilde{\mathbf{X}}_{l,1}^{(i-1)}\\ \widetilde{\mathbf{X}}_{l,2}^{(i-1)}\end{bmatrix}\right)\right\|_F^2,\end{aligned} \tag{S.6}$$

where $\mathbf{x}_{l,m}$ and $\mathbf{x}_{l,m}^{(i-1)}$ are the lth high-quality and degraded images of the mth material, respectively, for $l=1,\ldots,L$ and $m=1,2$, $\widetilde{\mathbf{X}}_{l,m}\in\mathbb{R}^{R\times N}$ and $\widetilde{\mathbf{X}}_{l,m}^{(i-1)}\in\mathbb{R}^{R\times N}$ are matrices whose columns are vectorized patches extracted from images $\mathbf{x}_{l,m}$ and $\mathbf{x}_{l,m}^{(i-1)}$ (with a spatial patch stride of 1×1), respectively. See related notations in (1), (5), and Section II.D.

Proof. Based on Proposition S.1, we obtain the result as follows:

$$\begin{aligned}&\frac{1}{2L}\sum_{l=1}^{L}\left\|\begin{bmatrix}\mathbf{x}_{l,1}\\ \mathbf{x}_{l,2}\end{bmatrix}-\begin{bmatrix}\sum_{k=1}^{K}\sum_{n=1}^{2}\mathbf{d}_{1,n,k}*\mathcal{T}_{\exp(\alpha_{n,k})}\left(\sum_{m=1}^{2}\mathbf{e}_{n,m,k}*\mathbf{x}_{l,m}^{(i-1)}\right)\\ \sum_{k=1}^{K}\sum_{n=1}^{2}\mathbf{d}_{2,n,k}*\mathcal{T}_{\exp(\alpha_{n,k})}\left(\sum_{m=1}^{2}\mathbf{e}_{n,m,k}*\mathbf{x}_{l,m}^{(i-1)}\right)\end{bmatrix}\right\|_2^2\\
=&\frac{1}{2L}\sum_{l=1}^{L}\left\|\begin{bmatrix}\mathbf{x}_{l,1}\\ \mathbf{x}_{l,2}\end{bmatrix}-\right.\\
&\left.\frac{1}{R}\begin{bmatrix}\sum_{j=1}^{N}\mathbf{P}_j^\top\mathbf{D}_{1,1}\mathcal{T}_{\exp(\boldsymbol{\alpha}_1)}\left(\mathbf{E}_{1,1}\mathbf{P}_j\mathbf{x}_{l,1}^{(i-1)}+\mathbf{E}_{1,2}\mathbf{P}_j\mathbf{x}_{l,2}^{(i-1)}\right)+\sum_{j=1}^{N}\mathbf{P}_j^\top\mathbf{D}_{1,2}\mathcal{T}_{\exp(\boldsymbol{\alpha}_2)}\left(\mathbf{E}_{2,1}\mathbf{P}_j\mathbf{x}_{l,1}^{(i-1)}+\mathbf{E}_{2,2}\mathbf{P}_j\mathbf{x}_{l,2}^{(i-1)}\right)\\ \sum_{j=1}^{N}\mathbf{P}_j^\top\mathbf{D}_{2,1}\mathcal{T}_{\exp(\boldsymbol{\alpha}_1)}\left(\mathbf{E}_{1,1}\mathbf{P}_j\mathbf{x}_{l,1}^{(i-1)}+\mathbf{E}_{1,2}\mathbf{P}_j\mathbf{x}_{l,2}^{(i-1)}\right)+\sum_{j=1}^{N}\mathbf{P}_j^\top\mathbf{D}_{2,2}\mathcal{T}_{\exp(\boldsymbol{\alpha}_2)}\left(\mathbf{E}_{2,1}\mathbf{P}_j\mathbf{x}_{l,1}^{(i-1)}+\mathbf{E}_{2,2}\mathbf{P}_j\mathbf{x}_{l,2}^{(i-1)}\right)\end{bmatrix}\right\|_2^2\\
=&\frac{1}{2LR^2}\sum_{l=1}^{L}\left\|\begin{bmatrix}\sum_{j=1}^{N}\mathbf{P}_j^\top\mathbf{P}_j\mathbf{x}_{l,1}\\ \sum_{j=1}^{N}\mathbf{P}_j^\top\mathbf{P}_j\mathbf{x}_{l,2}\end{bmatrix}-\right.\\
&\left.\begin{bmatrix}\sum_{j=1}^{N}\mathbf{P}_j^\top\left(\mathbf{D}_{1,1}\mathcal{T}_{\exp(\boldsymbol{\alpha}_1)}\left(\mathbf{E}_{1,1}\mathbf{P}_j\mathbf{x}_{l,1}^{(i-1)}+\mathbf{E}_{1,2}\mathbf{P}_j\mathbf{x}_{l,2}^{(i-1)}\right)+\mathbf{D}_{1,2}\mathcal{T}_{\exp(\boldsymbol{\alpha}_2)}\left(\mathbf{E}_{2,1}\mathbf{P}_j\mathbf{x}_{l,1}^{(i-1)}+\mathbf{E}_{2,2}\mathbf{P}_j\mathbf{x}_{l,2}^{(i-1)}\right)\right)\\ \sum_{j=1}^{N}\mathbf{P}_j^\top\left(\mathbf{D}_{2,1}\mathcal{T}_{\exp(\boldsymbol{\alpha}_1)}\left(\mathbf{E}_{1,1}\mathbf{P}_j\mathbf{x}_{l,1}^{(i-1)}+\mathbf{E}_{1,2}\mathbf{P}_j\mathbf{x}_{l,2}^{(i-1)}\right)+\mathbf{D}_{2,2}\mathcal{T}_{\exp(\boldsymbol{\alpha}_2)}\left(\mathbf{E}_{2,1}\mathbf{P}_j\mathbf{x}_{l,1}^{(i-1)}+\mathbf{E}_{2,2}\mathbf{P}_j\mathbf{x}_{l,2}^{(i-1)}\right)\right)\end{bmatrix}\right\|_2^2\\
\leq&\frac{1}{2LR}\sum_{l=1}^{L}\sum_{j=1}^{N}\left\|\begin{bmatrix}\widetilde{\mathbf{X}}_{l,1,j}\\ \widetilde{\mathbf{X}}_{l,2,j}\end{bmatrix}-\begin{bmatrix}\mathbf{D}_{1,1}&\mathbf{D}_{1,2}\\ \mathbf{D}_{2,1}&\mathbf{D}_{2,2}\end{bmatrix}\mathcal{T}_{\exp(\boldsymbol{\alpha})}\left(\begin{bmatrix}\mathbf{E}_{1,1}&\mathbf{E}_{1,2}\\ \mathbf{E}_{2,1}&\mathbf{E}_{2,2}\end{bmatrix}\begin{bmatrix}\widetilde{\mathbf{X}}_{l,1,j}^{(i-1)}\\ \widetilde{\mathbf{X}}_{l,2,j}^{(i-1)}\end{bmatrix}\right)\right\|_2^2\\
=&\frac{1}{2LR}\sum_{l=1}^{L}\left\|\begin{bmatrix}\widetilde{\mathbf{X}}_{l,1}\\ \widetilde{\mathbf{X}}_{l,2}\end{bmatrix}-\mathbf{D}\mathcal{T}_{\exp(\boldsymbol{\alpha})}\left(\mathbf{E}\begin{bmatrix}\widetilde{\mathbf{X}}_{l,1}^{(i-1)}\\ \widetilde{\mathbf{X}}_{l,2}^{(i-1)}\end{bmatrix}\right)\right\|_F^2,\end{aligned}$$

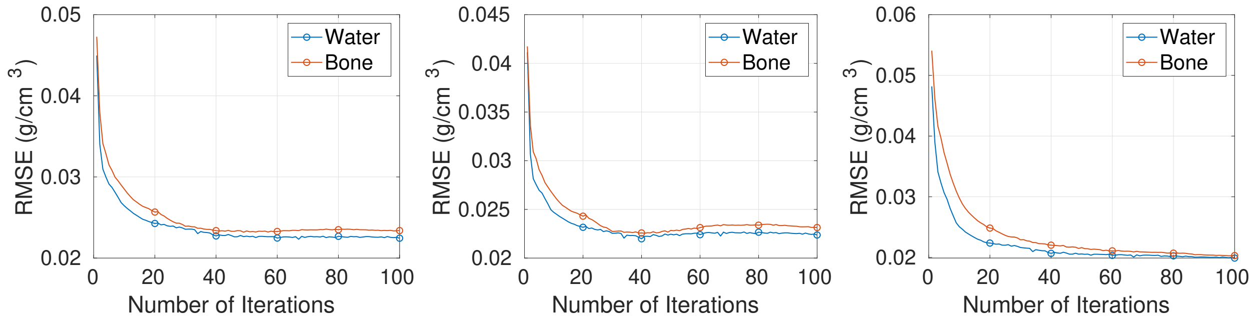

Figure S.1: RMSE plot of BCD-Net-dCNN for Test #1, Test #2, and Test #3, respectively.

where $\widetilde{\mathbf{X}}_{l,m,j}^{(i-1)} \in \mathbb{R}^R$ and $\widetilde{\mathbf{X}}_{l,m,j} \in \mathbb{R}^R$ are the jth column of $\widetilde{\mathbf{X}}_{l,m}^{(i-1)}$ and $\widetilde{\mathbf{X}}_{l,m}$, respectively. Here, the inequality holds by $\widetilde{\mathbf{P}}\widetilde{\mathbf{P}}^\top \preceq R \cdot \mathbf{I}$ with $\widetilde{\mathbf{P}} := [\mathbf{P}_1^\top, \cdots, \mathbf{P}_N^\top]^\top$.

S.III Supplementary Results for Section III

Figure S.1 shows the RMSE plots of water and bone images for BCD-Net-dCNN. BCD-Net-dCNN becomes overfitted around 40th iteration for test slices #1 and #2.

We generated ten different noise realizations to obtain NPS images for XCAT phantom data. We calculated the averaged NPS measure[4], denoted as $\overline{\text{NPS}}$, for each method using

$$\overline{\text{NPS}} = \frac{\sum_{i=1}^{10} |\text{DFT}\{f_i - f^*\}|^2}{10},$$

where f_i denotes the decomposed water image from the ith noise realization, and f^* denotes the ground truth of water image. Figure S.2 compares the magnitude of $\overline{\text{NPS}}$ from different methods. Across all frequencies, the NPS magnitude of BCD-Net-sCNN-hc is significantly smaller than those of direct matrix inversion, DECT-EP, DECT-ST, and dCNN. Furthermore, BCD-Net-sCNN-hc gives fewer vertical and horizontal frequency strips with lower intensity, compared to BCD-Net-sCNN-lc and BCD-Net-dCNN. The aforementioned NPS comparisons demonstrate the superiority of the proposed BCD-Net-sCNN-hc method in removing noise and artifacts inside soft tissue regions.

Figure S.3 and Figure S.4 show another two test slices comparisons. DCNN improves decomposition quality compared to DECT-EP and DECT-ST in terms of reducing noise and artifacts, but it still retains some streak artifacts. Compared to DCNN, BCD-Net-sCNN-hc further removes noise and artifacts, and improves the sharpness of edges in soft tissue.

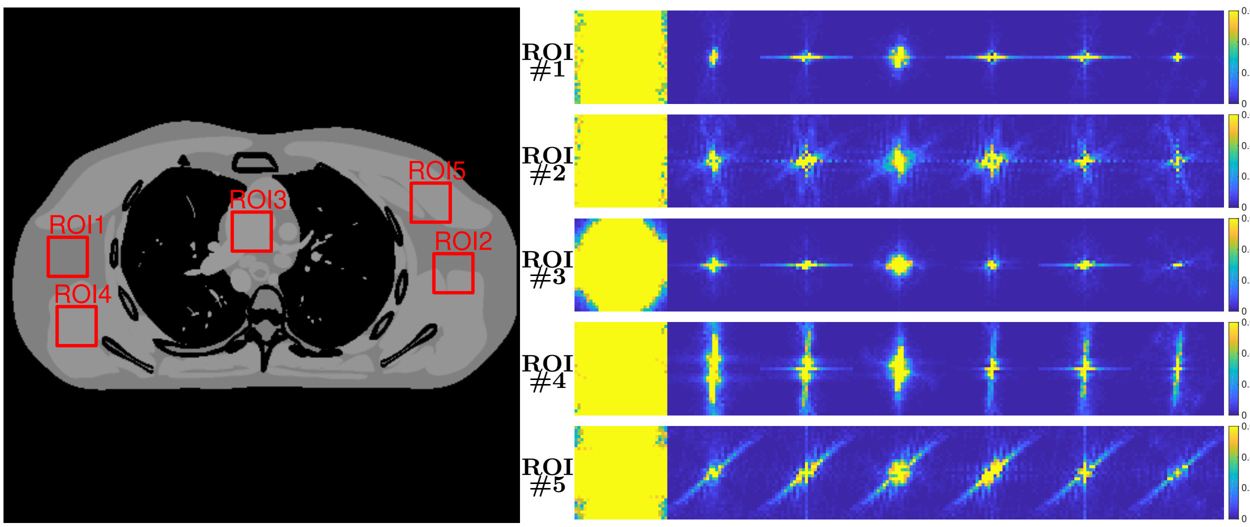

(a) (b)

Figure S.2: (a) Five selected ROIs indicated for $\overline{\text{NPS}}$ calculation for the decomposed water image of XCAT phantom. (b) Left to right: NPS measured within ROIs of decomposed water images obtained by direct matrix inversion, DECT-EP, DECT-ST, dCNN, BCD-Net-dCNN, BCD-Net-sCNN-lc, and BCD-Net-sCNN-hc. The first to the fifth rows in (b) show the $\overline{\text{NPS}}$ of the first to fifth ROIs, respectively, with display windows [0 0.6] g^2/cm^6.

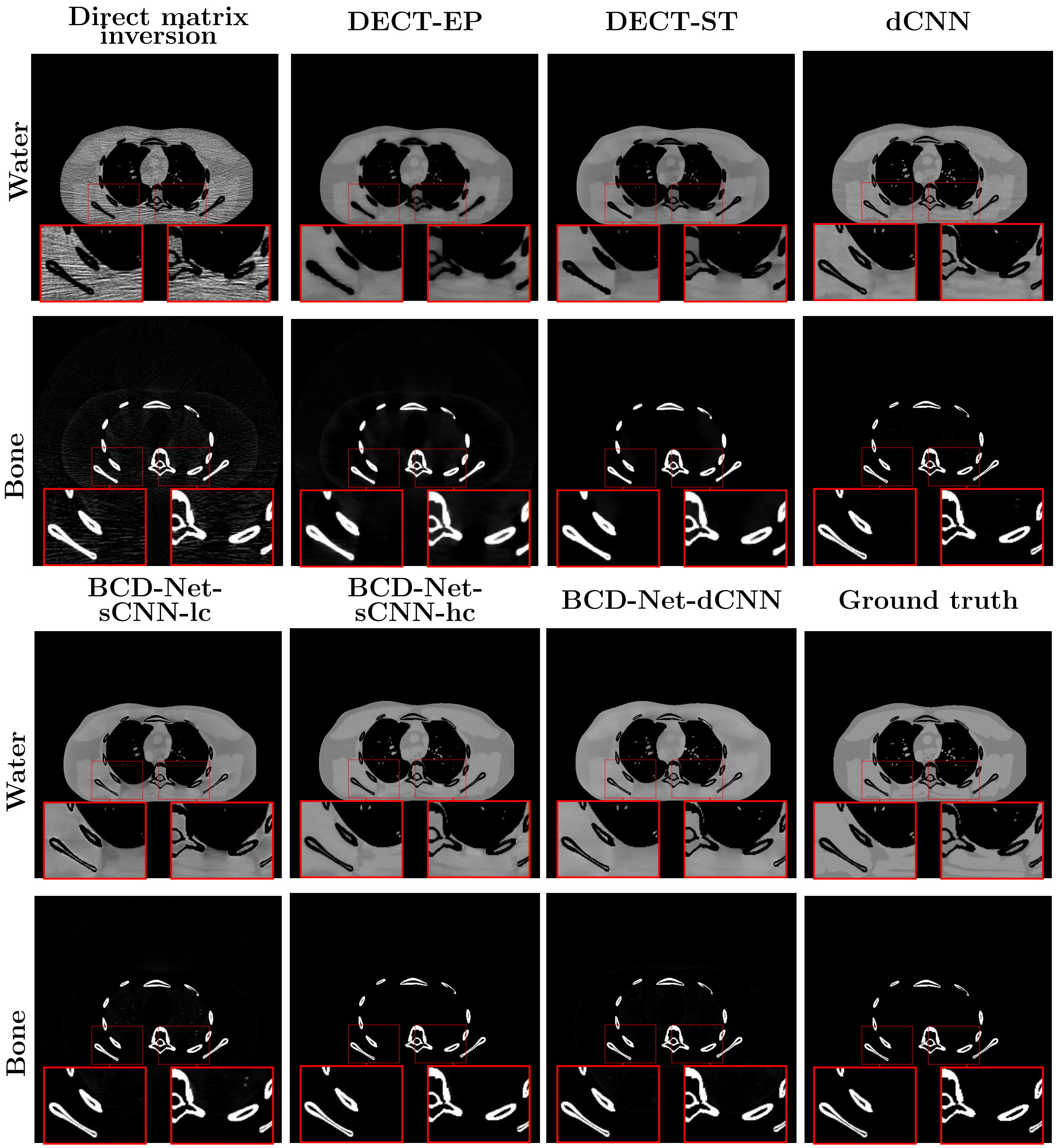

Figure S.3: Comparison of decomposed images from different methods (XCAT phantom test slice #2). Water and bone images are shown with display windows [0.7 1.3] $\mathrm{g/cm^3}$ and [0 0.8] $\mathrm{g/cm^3}$, respectively.

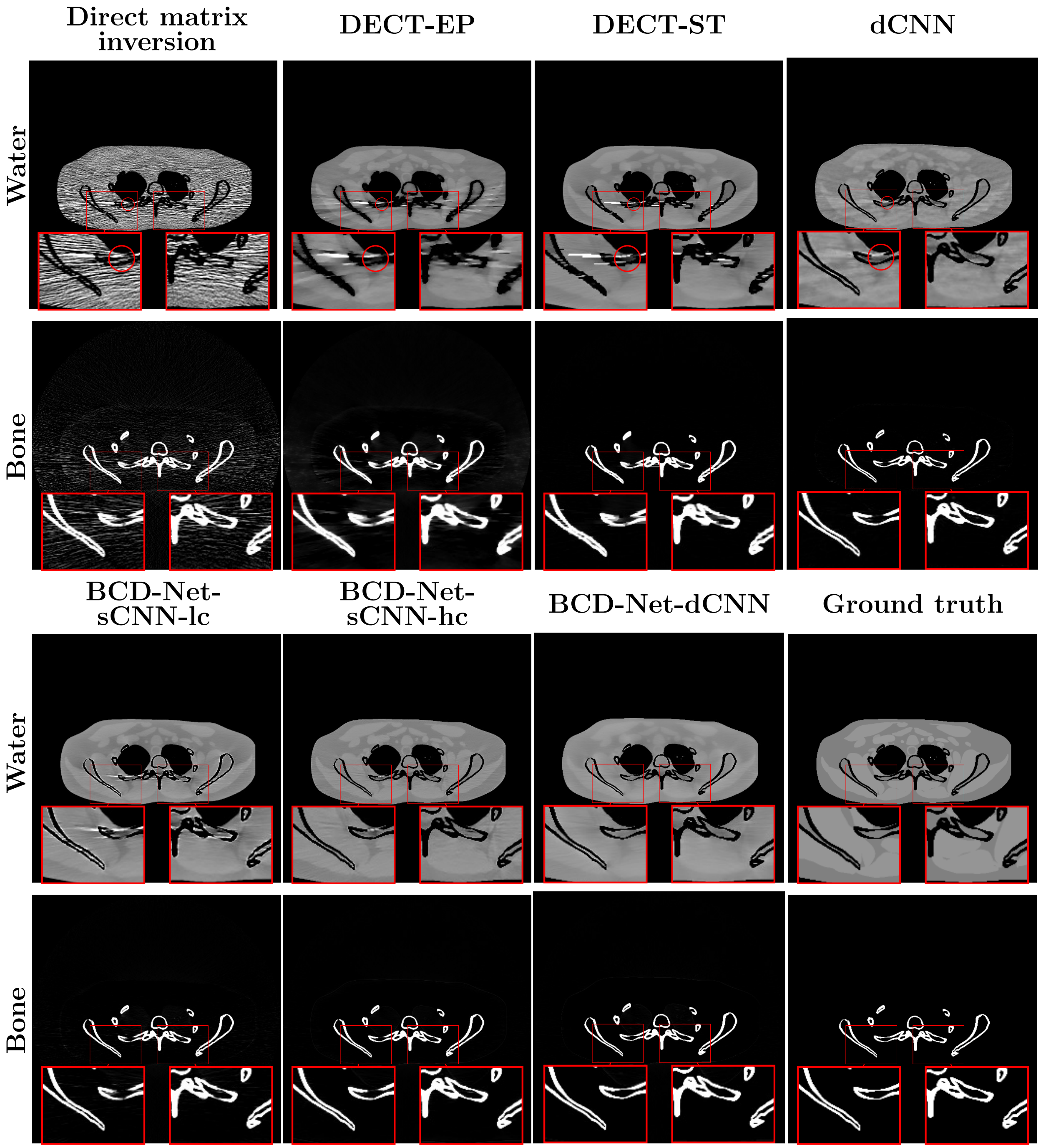

Figure S.4: Comparison of decomposed images from different methods (XCAT phantom test slice #3). Water and bone images are displayed with windows [0.7 1.3] $\mathrm{g/cm^3}$ and [0 0.8] $\mathrm{g/cm^3}$, respectively.

We ran additional three-material (fat, muscle, and bone) decomposition experiments with the proposed architecture, BCD-Net-sCNN-hc. We obtained the three initial decomposed images from high- and low-energy attenuation images, by using a Tikhonov-regularized direct matrix inversion method, i.e., $\mathbf{x}^{(0)} = (\mathbf{A}'\mathbf{A} + \lambda\mathbf{I})^{-1}\mathbf{A}'\mathbf{y}$ (three-material decomposition in dual-energy CT is an under-determined inverse problem). Figure S.5 compares #1 material density images from regularized direct matrix inversion, BCD-Net-sCNN-hc, and ground truth. The regularized direct matrix inversion method suffers from severe noise and artifacts, and does not decompose fat and muscle images. BCD-Net-sCNN-hc achieves significantly better three-material decomposition performance over the regularized direct matrix inversion method. Figure S.6 shows the RMSE convergence behavior of BCD-Net-sCNN-hc: similar to the RMSE convergence behavior in dual-material decomposition (see Figure 6), it decreases monotonically. Figure S.7 compares decomposed bone images and their error maps from dual- and three-material decomposition BCD-Net-sCNN-hc. (Note that ground-truth bone images are identical between the dual- and three-material decomposition cases.) The dual-material decomposition BCD-Net architecture achieves smaller errors and clearer image edges and structures, compared to the three-material decomposition BCD-Net method; see error maps and zoom-ins in bone images. This is natural because the initial decomposed images from the dual-material decomposition case are more accurate than those from the three-material decomposition case, and $\mathbf{A}_0$ in (P0) in dual-material decomposition is better conditioned than the counterpart in three-material decomposition in DECT.

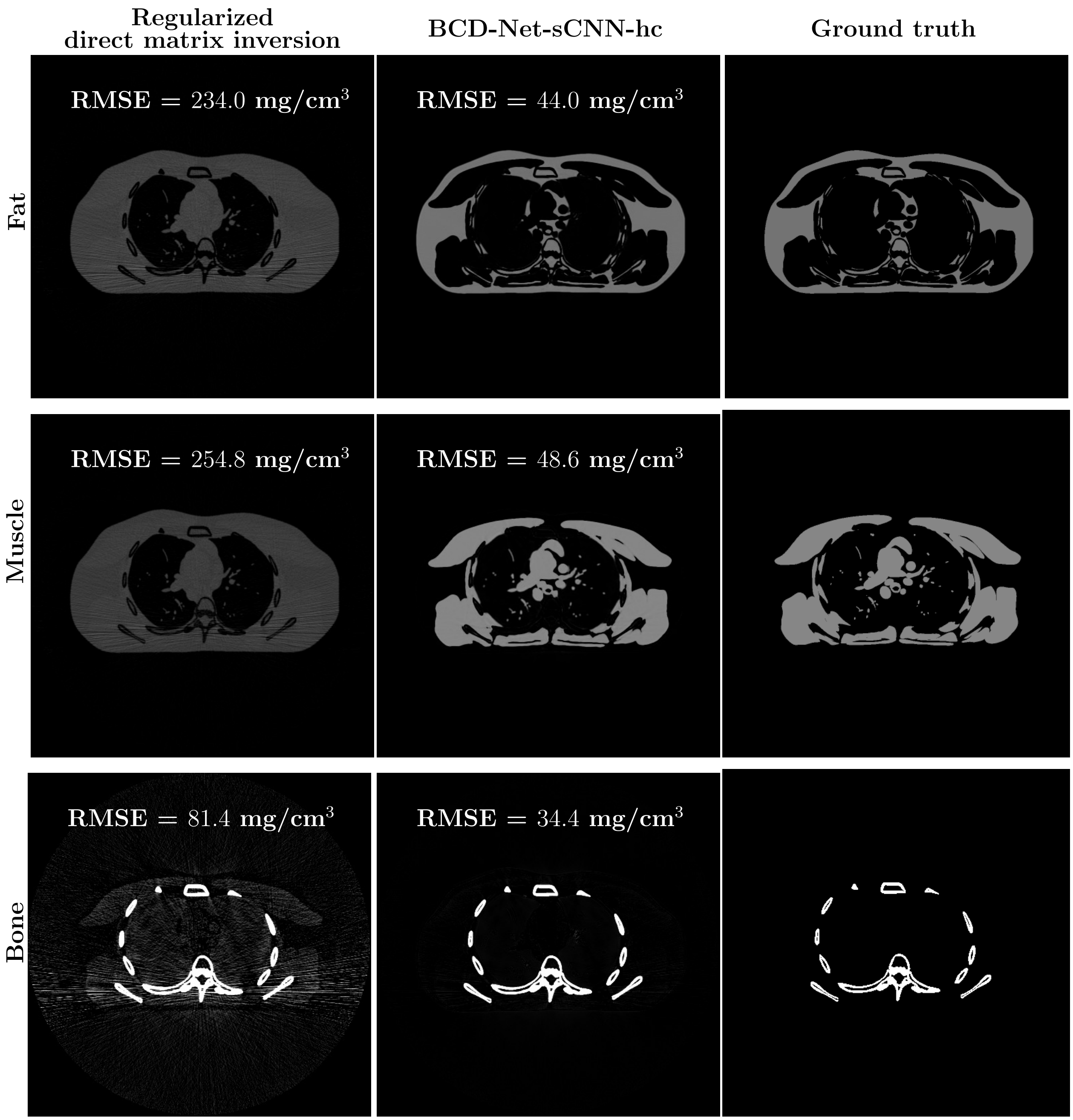

Figure S.5: Comparison of three decomposed images from regularized direct matrix inversion ($\lambda = 1 \times 10^{-5}$), BCD-Net-sCNN-hc, and ground truth. Fat, muscle, and bone images are shown with display windows [0 2] g/cm^3, [0 2] g/cm^3, and [0 0.5] g/cm^3, respectively.

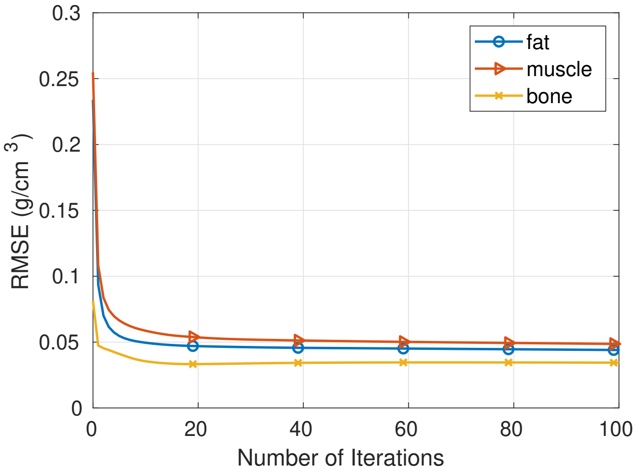

Figure S.6: RMSE convergence behaviors of three-material decomposition BCD-Net-sCNN-hc.

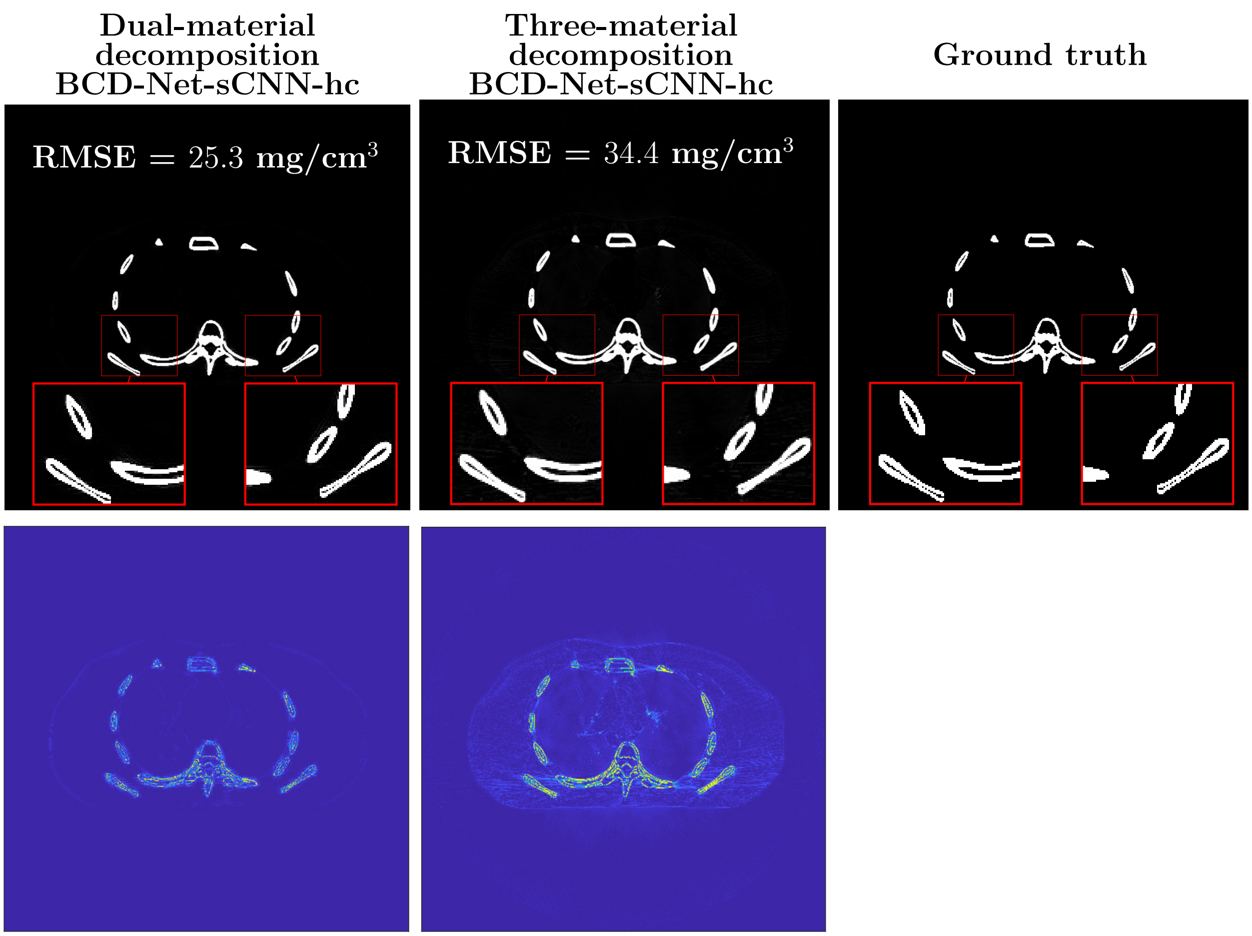

Figure S.7: Comparisons of decomposed bone images (display window [0 0.5] g/cm^3) and their error maps (display window [0 0.3] g/cm^3) from dual- and three-material decomposition BCD-Net-sCNN-hc architectures.

References

[1] Z. Li, Y. Long, and I. Y. Chun, An Improved Iterative Neural Network for High-Quality Image-Domain Material Decomposition in Dual-Energy CT, submitted (2021).

[2] I. Y. Chun and J. A. Fessler, Convolutional analysis operator learning: Acceleration and convergence, IEEE Trans. Im. Proc. **29**, 2108–2122 (2020).

[3] I. Y. Chun, Z. Huang, H. Lim, and J. A. Fessler, Momentum-Net: Fast and convergent iterative neural network for inverse problems, early access in IEEE Trans. Pattern Anal. Mach. Intell. (2020), DOI: 10.1109/TPAMI.2020.3012955.

[4] K. Li, J. Tang, and G. H. Chen, Statistical model based iterative reconstruction (MBIR) in clinical CT systems: experimental assessment of noise performance, Med. Phys. **41**, 041906 (2014).